

mRNA lipid nanoparticle phase transition

Marius F. W. Trollmann^{1,2} and Rainer A. Böckmann^{1,2,*}

¹Computational Biology, Department of Biology, Friedrich-Alexander-Universität Erlangen-Nürnberg, Erlangen, Germany and ²Erlangen National Center for High-Performance Computing (NHR@FAU), Erlangen, Germany

ABSTRACT Crucial for mRNA-based vaccines are the composition, structure, and properties of lipid nanoparticles (LNPs) as their delivery vehicle. Using all-atom molecular dynamics simulations as a computational microscope, we provide an atomistic view of the structure of the *Comirnaty* vaccine LNP, its molecular organization, physicochemical properties, and insight in its pH-driven phase transition enabling mRNA release at atomistic resolution. At physiological pH, our simulations suggest an oil-like LNP core that is composed of the aminolipid ALC-0315 and cholesterol (ratio 72:28). It is surrounded by a lipid monolayer formed by distearoylphosphatidylcholine, ALC-0315, PEGylated lipids, and cholesterol at a ratio of 22:9:6:63. Protonated aminolipids enveloping mRNA formed inverted micellar structures that provide a shielding and likely protection from environmental factors. In contrast, at low pH, the *Comirnaty* lipid composition instead spontaneously formed lipid bilayers that display a high degree of elasticity. These pH-dependent lipid phases suggest that a change in pH of the environment upon LNP transfer to the endosome likely acts as trigger for cargo release from the LNP core by turning aminolipids inside out, thereby destabilizing both the LNP shell and the endosomal membrane.

SIGNIFICANCE mRNA-based vaccines have tremendous therapeutic potential in the prevention of severe SARS-CoV-2 infections. Lipid nanoparticles (LNPs) act as carrier system for mRNA, protecting nucleotides against premature degradation and allowing for efficient release into target cells. Despite the decisive role of LNPs for the successful delivery of mRNA and thus for the action of vaccines, little is known about the molecular architecture of LNPs used within SARS-CoV-2 vaccines. Our molecular dynamics simulations of both lipid model systems and whole LNPs with the lipid composition used in the BioNTech & Pfizer vaccine offer unique insights into the structure of lipid nanoparticles at the atomistic scale and suggest a mechanism with an aminolipid acting as pH-sensitive switch for the delivery of mRNA-based drugs.

INTRODUCTION

Early on, the crucial role of lipid formulations including cationic, unfortunately typically toxic lipids, for the transfection of cells with RNA was recognized (1). The formulation of messenger RNA (mRNA) strands within lipid nanoparticles (LNPs) prevents early degradation of the nucleotides and increases the transfection rate for vaccines (2,3). Different lipid compositions were investigated to optimize the efficacy and safety of nanoparticles for drug delivery including also the design of novel molecular structures (4,5). A huge step forward toward less cytotoxic LNPs showing less unspecific interactions was made by utilizing a titratable cationic aminolipid for RNA encapsulation (6,7). Apart from the aminolipid, most modern LNPs

include a PEGylated lipid, cholesterol, and a standard phospholipid to effectively encapsulate and deliver mRNA (8). The PEGylated lipid is usually composed of a hydrophobic lipid-like anchor with a polyethylene glycol (PEG) chain attached to the headgroup (9). The polymers prevent the aggregation of LNPs during the shelf time of the vaccine as well as early neutralization by freely circulating immunocytes after administration (9,10).

mRNA-based vaccines play a vital role in fighting COVID-19 (11). Along with the conventional available vaccine platforms, mRNA-based vaccines were among the first authorized vaccines against SARS-CoV-2 and were applied for the first time to a larger part of the population. They transfer nucleoside-modified mRNA encoding the SARS-CoV-2 spike protein into the cytoplasm of human cells. The mRNA strands are then translated to a functional protein by the cell's own ribosomal machinery. The spike protein is usually found on the viral envelope to mediate the entry of the virus into the host cell via its interaction with

Submitted April 11, 2022, and accepted for publication August 25, 2022.

*Correspondence: rainer.boeckmann@fau.de

Editor: Siewert Jan Marrink.

<https://doi.org/10.1016/j.bpj.2022.08.037>

© 2022 Biophysical Society.

This is an open access article under the CC BY-NC-ND license (<http://creativecommons.org/licenses/by-nc-nd/4.0/>).



the angiotensin-converting enzyme 2 receptor (12,13). Its exposed position as well as its crucial role in viral transfection makes it a predestined target for an effective immune response. Neutralizing antibodies binding to the spike protein would not only mark the virus but would also prevent it from entering a cell. Two LNP-based mRNA vaccines which showed a high efficacy against SARS-CoV-2 in their third clinical trial were *Comirnaty* (95% (14), BioNTech & Pfizer) and *Elasomeran* (94.1% (15), Moderna).

Cationic lipids as a component of vaccine LNPs should in particular ensure a high encapsulation rate for mRNA. Transmission cryo-electron microscopy (cryo-TEM) images, coarse-grained simulations, and small-angle scattering (SAS) experiments indeed indicated that various ionizable cationic lipids (e.g., 2,2-dilinoleyl-4-(2-dimethylaminoethyl)-(1,3)-dioxolane (DLin-KC2-DMA, abbreviated as KC2) or heptatriaconta-6,9,28,31-tetraen-19-yl 4-(dimethylamino)butanoate (DLin-MC3-DMA, abbreviated as MC3)) form inverted micelle-like structures around mRNA within the LNP core (16–18). Protonation of aminolipids at low pH presumably results in binding to the negatively charged backbone of the nucleotides. Subsequent deprotonation at neutral pH then causes a neutral surface charge and thereby minimizes LNP toxicity. Upon delivery of LNPs to the acidic endosome, ionization of LNPs is expected to result in structural changes, presumably leading to disruption of the endosomal membrane and thus delivery of the mRNA cargo to the cytosol (7,10).

While a number of studies addressed the properties of LNPs including KC2 or MC3 lipids, the characteristics of *Comirnaty* LNPs including the titratable aminolipid ALC-0315 was rarely investigated, despite the conspicuous structure of ALC-0315 with its four fatty acyl chains compared with two for other standard aminolipids and phospholipids: A recent computational study by Paloncýová et al. (19) reported an increased disorder for preassembled bilayers containing cationic lipids and non-lamellar phases with a separation between 1,2-distearoyl-*sn*-glycero-3-phosphocholine (DSPC)/cholesterol and regions rich in the aminolipid in its neutral form. However, the structure of the *Comirnaty* LNPs, in particular whether the LNP core is surrounded by a monolayer (17) or a bilayer (20,21), as well as the composition of shell and core domains, are still largely uncharted territory.

In this study, we investigated how a change in pH results in a dramatic structural transition of the mRNA LNP formulation used in the *Comirnaty* vaccine. Atomistic molecular dynamics (MD) simulations provide unique insight into self-organization of the LNP formulation, the composition and structure of the LNP core and shell, and mRNA enclosure in the LNP formulation. The *Comirnaty* LNPs are characterized by an unstructured oil-like core region that is surrounded by a DSPC/cholesterol lipid monolayer close to the cholesterol solubility limit that includes PEGylated lipids and aminolipids in their neutral form. Our results pro-

vide a new perspective on the molecular organization of LNPs and suggest a mechanism for the initial steps of mRNA release from the LNP to the cytoplasm.

MATERIALS AND METHODS

Molecular dynamics simulation

General parameters

The topologies of cholesterol and DSPC as well as the parameterization for the inter- and intra-atomic interactions were obtained from the CHARMM36 force field (July 2020) (22,23). Since there were no topologies available for ALC-0315 and ALC-0159 (PEGylated lipid with 45 PEG units in lipid headgroup), the CGENFF (24,25) webserver was used to generate the respective files based on already known molecular building blocks (see Tables S1–S4 for the penalty scores).

All systems were energy minimized using a steepest descent algorithm either with a convergence limit of 1000 kJ/(mol × nm) or a given number of steps. During the simulations, the temperature was kept constant with the Nosé-Hoover thermostat (26,27) with a temperature coupling constant of 1.0 ps. A reference pressure of 1 bar with a pressure coupling constant of 5.0 ps and a compressibility of $4.5 \times 10^{-5} \text{ bar}^{-1}$ was applied in all simulations. The Berendsen barostat (28) was chosen during the preparation of the systems because of its higher numerical stability. For production runs, the barostat was changed to the Parrinello-Rahman barostat (29), since it better represents the NPT ensemble. For the van der Waals interactions, a force-based switch function (1.0–1.2 nm) was used, while the long-range Coulomb interactions were handled by using the particle-mesh Ewald method (30). The bonds between heavy atoms and hydrogens were constrained with the LINCS algorithm (31) using a LINCS order of 4 with one iteration step. Unless otherwise stated, a time step of 2 fs and a reference temperature of 310 K were used in the simulations. The CHARMM TIP3P (23,32) water model was used. The software package GROMACS (v2019.3) (33) was deployed to prepare, execute, and analyze the simulations. Custom codes were written employing the MDAnalysis library (34,35) for more specific analysis. All input parameters, topologies, and structures are available via Zenodo at <https://doi.org/10.5281/zenodo.7037843>.

Simulation systems

Configuration of Comirnaty lipid mixture at low and neutral pH. Spontaneous aggregation and structure formation was studied for a fully hydrated system mimicking the lipid composition of *Comirnaty* LNPs (46.3:9.4:42.7:1.6) (3) (system A in Table 1). All aminolipids were chosen to be protonated, thus matching a condition well below their pK_a of 6.09 (4); the charge of all other lipids was kept unchanged (pK_a of phosphatidylcholine (PC) lipids is below 1 (36)). The salt concentration was chosen as 150 mM NaCl. The bending modulus was analyzed from a quadruplicated system (system B in Table 1).

For comparison of the lipid bilayer characteristics, a membrane consisting of DSPC and cholesterol was studied. The amount of cholesterol was kept at a similar level of 43 mol %. This system with 770 DSPC and 580 cholesterol molecules was set up and simulated for a total of 1.3 μs (system C in Table 1). The effect of neutral pH on the *Comirnaty* lipid mixture was studied by deprotonation of the aminolipids (system D in Table 1) within the equilibrated membrane system (system B). Owing to the decreased surface area of the membrane, the water content was reduced to 42 water molecules per lipid to increase the computational efficiency.

The embedment of short mRNA strands into *Comirnaty* LNPs was addressed in spontaneous self-assembly simulations of the above 4-lipid mixture (at low pH condition) with short mRNA strands: The initial structure of a short section (CCUUUUGAGAGAGAUUUUC) of the mRNA

TABLE 1 Summary of main simulation systems used in the present work

System	ALC-0315:DSPC:Chol:ALC-0159:mRNA	Simulation time (μ s)	Objective
A	122:24:112:6:0	4.1; 3.0; 3.0	self-assembly of <i>Comirnaty</i> lipids
B	488:96:448:24:0	1	bending modulus of <i>Comirnaty</i> membrane
C	0:770:580:0:0	1.3	bulk properties of DSPC:Chol system
D	488:96:448:24:0	0.633	influence of deprotonation on LNP
E	488:96:448:24:4	4.0; 5.0; 1.0; 1.0	self-assembly of <i>Comirnaty</i> lipids and mRNA
F	7808:1536:7168:384:0	0.240; 0.445; 0.456	<i>Comirnaty</i> LNP without PEG
G	7808:1536:7168:384:0	0.665	<i>Comirnaty</i> LNP with PEG

sequence encoding the spike protein of SARS-CoV-2 (RefSeq: NC_045512.2, position 22,949–22,968, accessed June 7, 2022) was prepared with AMBER (37) (the full length of the *Comirnaty* mRNA is ≈ 4000 (38)). According to the modifications of the administered vaccine each uridine was exchanged with N¹-methylpseudouridine (14). Parameters for the nucleotides were taken from the CHARMM36 force field (39,40). The structure was slowly relaxed in two preparation runs including position restraints (1000 kJ/(mol \times nm)) and increasing integration time steps (1 fs, 1.5 fs). In the last step, the mRNA strand was simulated without position restraints and with a time step of 2 fs for 0.1 μ s to allow an unbiased equilibration of the sequence in solvent. The single mRNA strand was solvated in a box with randomly placed lipids (similar to system A) and simulated for 0.44 μ s with all aminolipids protonated (two replicas). Subsequently, different sets of aminolipids were deprotonated to model a sudden increase to a neutral pH (for both replicas): In set 1, all aminolipids not facing the mRNA were deprotonated (> 1.2 nm distance from mRNA phosphates, 96 and 92 aminolipids deprotonated), in set 2, randomly selected aminolipids (same number of deprotonated lipids as in set 1) were deprotonated, and in set 3, all aminolipids were deprotonated. The simulation times with one mRNA strand ranged between 0.31 and 0.78 μ s. Final snapshots of mRNA-lipid systems with protonated aminolipids (sets 1 and 2) were quadruplicated and further equilibrated for 4 μ s and 5 μ s, respectively (set 1), and 1 μ s for replicas of set 2 (system E in Table 1).

Structure of lipid nanoparticles. Spherical all-atom LNPs were modeled based on results obtained for the *Comirnaty* LNP composition at neutral pH (system D in Table 1). Results for the latter system suggested that a hydrophobic LNP core is formed by aminolipids and cholesterol (ratio of 488:188) surrounded by a lipid monolayer shell composed of DSPC:cholesterol:ALC-0159 at a ratio of 96:260:24 (for details see results

and discussion). The spherical LNP was set up in the following sequential manner (compare Fig. 1).

Modeling of the LNP core started from a subsystem of the equilibrated *Comirnaty* lipid assembly (system D) that is suggested to model the hydrophobic LNP core region (488 aminolipids and 188 cholesterol molecules, Fig. 1 a). This cuboid model for the LNP core region was reshaped to a cube (Fig. 1 b). The resulting system was in total multiplied by 16 to reach a total LNP size estimated from the surface/volume ratio observed for a periodic membrane built in system D (see results and discussion, snapshots in Fig. 1, c–e, in total 7808 aminolipids and 3008 cholesterol molecules). The final cube was further equilibrated and reshaped to a sphere in vacuum (NVT ensemble) by application of a spherical flat-bottom potential (20 kJ/(mol \times nm), snapshot in Fig. 1 f). Subsequently, the lipids of the monolayer shell (in total 1536 DSPC molecules, 384 PEGylated lipids, 4160 cholesterol molecules) were randomly placed at least 2 nm above the surface of the hydrophobic LNP core with their tails always oriented toward the core of the LNP. The length of the PEG chain of ALC-0159 was initially reduced to two monomers. The shell was minimized with a soft-core potential to relax energetically unfavorable conformations. The energy minimization was followed by several equilibration steps in the NVT ensemble. The equilibrated structure of shell and core were solvated in a 150 mM NaCl solution. Solvent molecules placed between shell and core region were removed. The shell lipids quickly formed a stable lipid monolayer around the LNP core (snapshot in Fig. 1 g). After 523 ns of equilibration, the full-length PEG chains were modeled in a mushroom configuration to the anchors of ALC-0159 (snapshot in Fig. 1 h). The full LNP has a radius of ≈ 17.7 nm (without PEG chains).

The temperature was maintained by the v-rescale thermostat (42) with a coupling constant of 0.1 ps in the final production simulations. The

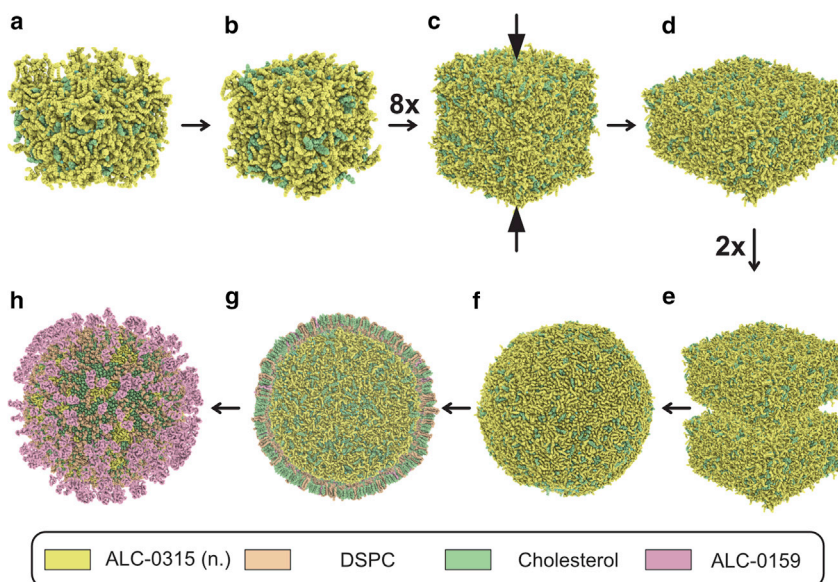


FIGURE 1 Snapshots of intermediate steps in construction of a *Comirnaty* LNP. An initial amino-lipid-cholesterol phase (a) was converted into a cube (b). The cube was subsequently replicated eight times to form a larger cube (c). A semi-isotropic pressure coupling scheme was applied to create a cuboid (d) that was duplicated (e). A spherical conformation was enforced by equilibration in vacuum in combination with flat-bottom potentials in (f). Surface lipids surrounding the core were modeled as a monolayer (g). Following equilibration, missing PEG chains were added to the structure (h). The images were created with PyMol (53). To see this figure in color, go online.

remaining parameters were equal to the parameters of the previous simulations. The GROMACS 2021 series (43) was used to prepare, execute, and analyze the simulations. Custom codes were written by employing the MDAnalysis library (34,35) for more specific analysis.

Analysis

Spatial lipid composition

The lipid composition in the monolayer and the core was obtained by fitting a spherical grid to the surface of the LNP. Grid points were placed on a unit sphere using the spiral method (44),

$$\begin{aligned}\theta_j &= \arccos\left(\frac{2j-1-J}{J}\right) \varphi_j \\ &= \sqrt{\pi J} \times \arcsin\left(\frac{2j-1-J}{J}\right),\end{aligned}$$

for $j = 1, \dots, J$. In the present work, a total of $J = 750$ grid points provided a sufficient trade-off between speed and accuracy. After the setup of the grid, each point was iteratively displaced along the inward normal of the sphere. An iteration was terminated if the grid point came into close contact (≤ 1.5 nm) with a lipid atom. The grid was subsequently interpolated by adding a midpoint between neighboring grid points, i.e., between all points with a distance ≤ 4.0 nm. Lipids with atoms within a distance of 2.5 nm from the grid were assumed to be part of the surrounding monolayer. The composition of the core was calculated by subtracting the number of lipids within the LNP shell from the total number of lipids in the simulation system.

Scattering intensity

SAS experiments are a ubiquitous tool for extracting information on the organization and shape of a particle. If X-rays are used for the experiment (i.e., SAXS), the scattering intensity depends on the distribution of electrons. SAXS data were reported in the past for a polydisperse solution of different LNPs (17,18,45). For comparison with the *Comimaty* LNPs studied here, we assumed a constant spherically symmetric electron density taken from our simulations. The following briefly recapitulates the underlying theory.

Since SAXS reports on the difference in scattering intensity to bulk water, and since molecules of interest (i.e., proteins, LNPs, and so forth) carry a solvation shell along with properties different from bulk water, the intensity of the displaced bulk water, $I_B(\mathbf{q})$, must be subtracted from the intensity $I_S(\mathbf{q})$ of the solvated solute to yield the SAXS scattering intensity $I(\mathbf{q})$:

$$I(\mathbf{q}) = I_S(\mathbf{q}) - I_B(\mathbf{q}). \quad (1)$$

\mathbf{q} is the scattering wave vector with a magnitude of

$$q = \frac{4\pi\sin(\theta)}{\lambda}. \quad (2)$$

The wave vector depends only on the scattering angle θ and the wavelength λ of the incident X-ray beam. The intensity $I(\mathbf{q})$ can be directly calculated from atomistic models by using the explicit positions of the atoms together with their atomic form factors. Park et al. (46) and Chen and Hub (47) showed that trajectories generated by MD simulations are suitable for computing reliable SAXS curves. The intensity is

$$\begin{aligned}I(\mathbf{q}) &= \langle |\langle \bar{S}(\mathbf{q}) - \bar{B}(\mathbf{q}) \rangle_\omega|^2 \rangle_\Omega + \left[\langle |\bar{S}(\mathbf{q})|^2 \rangle_\omega \right. \\ &\quad \left. - \langle |\bar{S}(\mathbf{q}) \rangle_\omega|^2 \right] - \left[\langle |\bar{B}(\mathbf{q})|^2 \rangle_\omega - \langle |\bar{B}(\mathbf{q}) \rangle_\omega|^2 \right] \rangle_\Omega, \quad (3)\end{aligned}$$

where $\bar{S}(\mathbf{q})$ and $\bar{B}(\mathbf{q})$ are the Fourier transforms of the electron densities of both the solute and its hydration layer and of the bulk water in the excluded volume, respectively. The average over a simulation trajectory is denoted as $\langle \dots \rangle_\omega$, while the spherical average $\langle \dots \rangle_\Omega$ takes all possible rotations of the solute into account. For a static continuous electron density, the above relation reduces to

$$I(q) = \langle |\langle \bar{S}(\mathbf{q}) - \bar{B}(\mathbf{q}) \rangle_\omega|^2 \rangle_\Omega. \quad (4)$$

The size and the shape of the simulated LNPs allow not only to assume a continuous but also a spherically symmetric distribution of electrons. Similarly, the density of the bulk water $\rho_{solvent}$ was taken as uniform. The electron density of the LNP with its hydration layer follows as

$$S(r) = S_L(r) + S_W(r), \quad (5)$$

where $S_L(r)$ and $S_W(r)$ are the radial electron densities of the LNP molecules and of the hydration shell, respectively. The electron density of the bulk water is expressed as

$$B(r) = \rho_{solvent} \times \mathbb{1}_{[0, R]}(r). \quad (6)$$

The indicator function $\mathbb{1}_{[0, R]}(r)$ sets the border of the volume containing the solute and the hydration layer. The spherical symmetry of the systems allows us to rewrite the intensity as (see also (48))

$$I(q) = \left(\langle \langle \bar{S}(q) \rangle_\omega \rangle_\Omega - \langle \langle \bar{B}(q) \rangle_\omega \rangle_\Omega \right)^2. \quad (7)$$

Both Fourier transforms are obtained from the integrals over the distance r from the center of symmetry (48),

$$\langle \langle \bar{S}(q) \rangle_\omega \rangle_\Omega = \int_0^\infty \langle S(r) \rangle_\omega \times \frac{\sin(qr)}{qr} \times 4\pi r^2 dr \quad \text{and} \quad (8)$$

$$\langle \langle \bar{B}(q) \rangle_\omega \rangle_\Omega = \int_0^\infty \langle B(r) \rangle_\omega \times \frac{\sin(qr)}{qr} \times 4\pi r^2 dr. \quad (9)$$

The integral for $\bar{S}(q)$ is solved numerically, e.g., with the integrate module of the scipy package (49). In the case of $\bar{B}(q)$, the integral has the analytical solution

$$\bar{B}(q) = \frac{4\pi\rho_{solvent}}{q^3} \times (\sin(qR) - \cos(qR) \times hR). \quad (10)$$

Eqs. 8 and 9 were employed to analyze the expected scattering intensity for a polydisperse LNP solution (Fig. 6 d), assuming that the LNP sizes follow a generalized extreme value distribution. The model parameters were estimated by comparison with cryo-TEM data and fit to SAXS data for MC3-LNPs (17). To validate our approach, we calculated the intensity pattern for a small LNP (half the number of lipids compared with system G and only two PEG monomers in the headgroup of ALC-0159) with Eqs. 8 and 9, respectively, and the method of Chen and Hub (47) (see Fig. S7).

Membrane bending modulus

The membrane bending modulus was calculated via the Helfrich-Canham theory of surface undulations (50,51). This method approximates a membrane as an elastic sheet without an internal structure, making it more suitable for membranes containing components with a non-standard structure. The surface of the elastic sheet was defined by the height field $h(x_i, y_j)$ of the lipid headgroups in the opposite leaflets as a function of the lateral coordinates x_i, y_j at grid points i, j . The power

spectrum $\langle |\bar{h}(\mathbf{q})|^2 \rangle$ of the height \bar{h} averaged over both leaflets was obtained by a two-dimensional fast Fourier transformation of $\bar{h}(x, y)$. $\langle |\bar{h}(\mathbf{q})|^2 \rangle$ was subsequently reduced to a one-dimensional representation by averaging intensities for which $|\mathbf{q}| = q$. The bending modulus K_C of the membrane can be extracted from a linear fit on the power spectrum with the equation

$$\langle |\bar{h}(q)|^2 \rangle = \frac{k_B T}{K_C \times q^4}, \quad (11)$$

where T is the temperature, and k_B the Boltzmann constant. The algorithm is described in more detail by Levine et al. (52).

RESULTS AND DISCUSSION

The structure of *Comirnaty* LNPs, their loading with mRNA, and pH-induced mechanisms governing potential mRNA release were studied employing atomistic MD simulations.

In a first step, the self-assembly of a complex lipid mixture in solvent was studied at low pH using the lipid composition of *Comirnaty* LNPs, in both the presence and absence of short mRNA fragments. The structural transition upon a sudden increase to neutral pH was initiated by deprotonation of all aminolipids for the mRNA-free case and selected aminolipids in the presence of mRNA. The system sizes were chosen to enable the formation of membrane-like phases (“LNP membrane”) across the periodic boundaries of the simulation systems, i.e., the system size is well below the size expected for LNPs (radius of tens of nanometers). The computational effort is thereby substantially reduced without altering the main characteristics, as was shown by Paloncýová et al. (19) and Ramezanzpour et al. (53).

In a second step, insights from these comparably small, membrane-like systems were used to guide the atomistic modeling and simulation of full LNPs.

Self-assembly of *Comirnaty* lipid composition at low pH

The lipid composition of the studied systems was chosen according to the molar fractions in the *Comirnaty* vaccine (3), i.e., the molar lipid ratio for ALC-0315:DSPC:cholesterol:ALC-0159 (PEGylated lipid) is 46.3:9.4:42.7:1.6. Spontaneous self-assembly of the lipids was initially studied for a cubic $10 \times 10 \times 10 \text{ nm}^3$ box containing the following numbers of randomly placed lipids: 122 protonated ALC-0315s, 24 DSPC molecules, 112 cholesterol molecules, and 6 ALC-0159 molecules solvated by ≈ 82 water molecules per lipid (Fig. 2 *a*, system A in Table 1). Metastable bilayer-like structures were established after 0.2–0.3 μs of simulation time (Fig. 2 *c*). The formation of stable lipid bilayers was accelerated by applying a temperature of 400 K (for 213 ns, see Fig. 2, *d* and *e*). The mass density of the lipids along the membrane normal analyzed from at least 3- μs -long all-atom

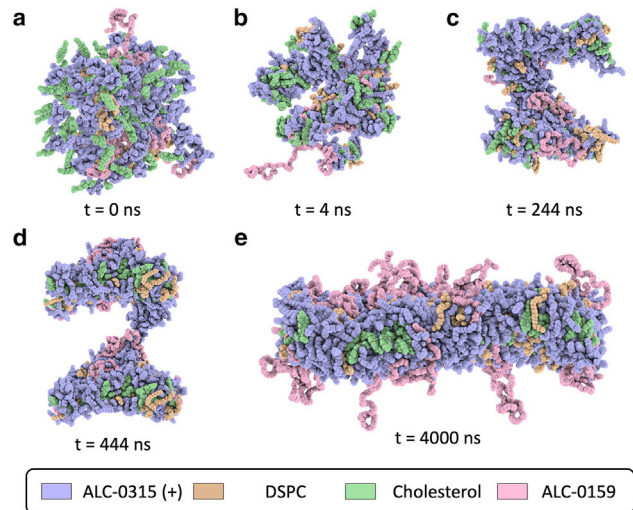


FIGURE 2 Self-assembly process of a membrane based on the lipid components inside the *Comirnaty* vaccine. Shown are snapshots of the initial random distribution of the lipids inside a cubic box (*a*) and the formation of intermediate structures observed after $t = 4 \text{ ns}$ (*b*) and $t = 244 \text{ ns}$ (*c*), and a snapshot during a temperature spike simulation at 400 K (*d*). Finally, (*e*) shows an intact bilayer-type structure after 1 μs equilibration of a quadruplicated structure (system B in Table 1). The lateral box size for the latter bilayer structure was approximately $19.1 \text{ nm} \times 19.1 \text{ nm}$. The images were created with PyMol (41). To see this figure in color, go online.

simulations shows a typical membrane morphology with the polar headgroups of all lipids oriented toward the solvent and the acyl chains forming the hydrophobic core (Fig. 3, *a* and *b*), overall comparable with a previous study that started from a bilayer configuration (19).

The DSPC lipids within the LNP mixture adopt a fluid conformation as suggested by the rather low deuterium order parameters of the DSPC acyl chains (Fig. 4, *a* and *b*, red curves). For comparison, a substantially increased packing density of DSPC lipids was observed for a binary DSPC/cholesterol membrane (43 mol % cholesterol) that is mirrored in increased order parameters (Fig. 4, *a* and *b*, blue curves). The packing of PC lipids with a high amount of cholesterol drives the binary membrane to adopt a liquid-ordered membrane phase (L_o) (54). In turn, the conical aminolipid in combination with a high amount of cholesterol pushes the LNP mixture to adopt a fluid-like phase even at ambient temperatures, despite the high melting temperature of $\approx 54^\circ\text{C}$ for DSPC.

The high flexibility of the lipids affects the elasticity of the membranes: The bending modulus K_C of the binary membrane was computed to $38.6 \pm 2.2 k_B T$ as compared with only $K_C = 4.3 \pm 0.3 k_B T$ for the more complex LNP membrane. This low bending modulus—also when compared with standard fluid-phase PC bilayers with bending moduli ranging between 13 and $28 k_B T$ for different saturated and monounsaturated acyl chains (55)—is likely beneficial for the (initial) packing of mRNA strands for

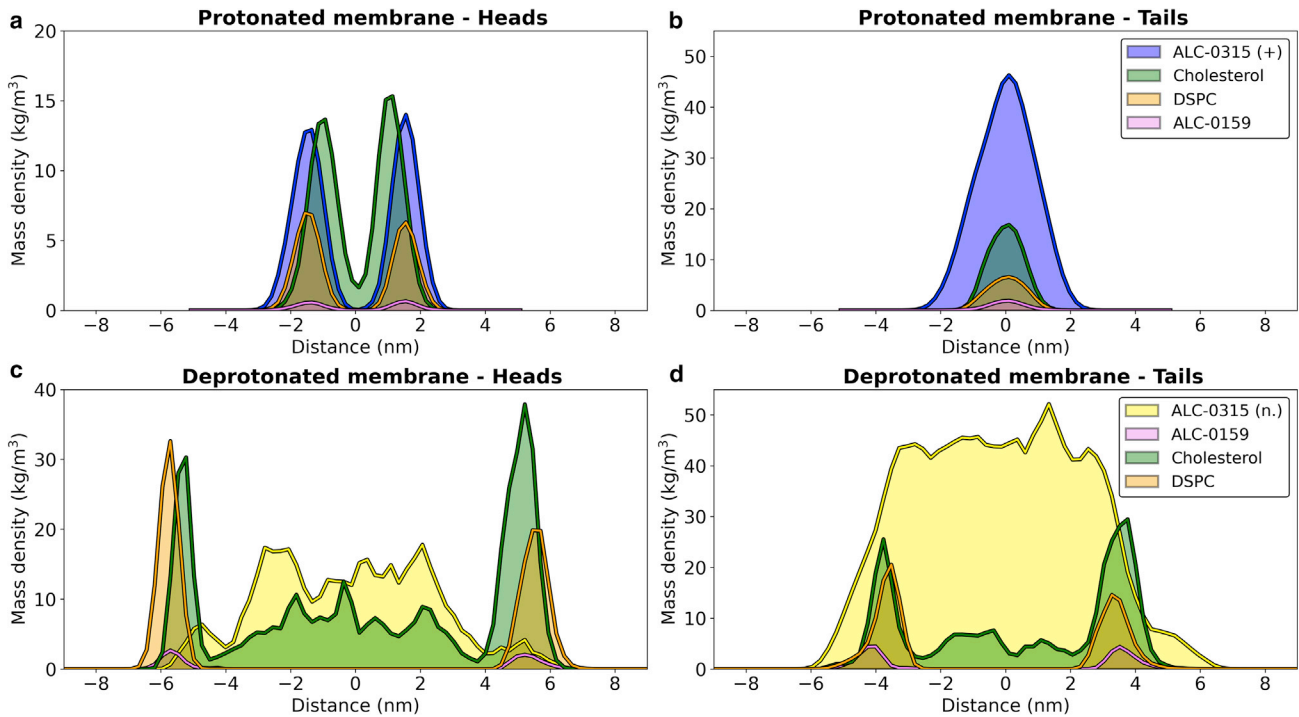


FIGURE 3 Mass density of the lipid headgroups (*a* + *c*, one atom per molecule) and of the lipid acyl chains (*b* + *d*, last carbon atom of each tail) of ALC-0159, ALC-0315, DSPC, and cholesterol for the protonated (*a* + *b*, system A) and deprotonated (*c* + *d*, system D) aminolipids along the membrane normal. To see this figure in color, go online.

vaccine LNPs, since it enables the formation of small vesicles with a high curvature.

pH-induced phase transition of *Comirnaty* bilayers

The influence of pH on the membrane phase was addressed by instantaneous deprotonation of the titratable cationic aminolipids within the equilibrated low-pH membrane patch (Fig. 5 *a*; system D in Table 1, see materials and methods). The loss of positive charge induced a rapid change in the morphology of

the bilayer. The increased hydrophobicity of the aminolipids at neutral pH as well as their conical shape (19) drives the neutralized lipids away from the membrane polar interface toward the hydrophobic core region (Fig. 5 *b*).

The fast depletion of the aminolipid from the lipid/solvent interface led to the formation of two stable and different phases: two decoupled and solvent-facing monolayers built mainly by DSPC, the PEGylated lipid (ALC-0159), and cholesterol that sandwich a thick apolar core region containing the aminolipids and cholesterol (Fig. 3, *c* and *d*). This phase transition at neutral pH is connected to a drastically increased shielding of the membrane surface by the

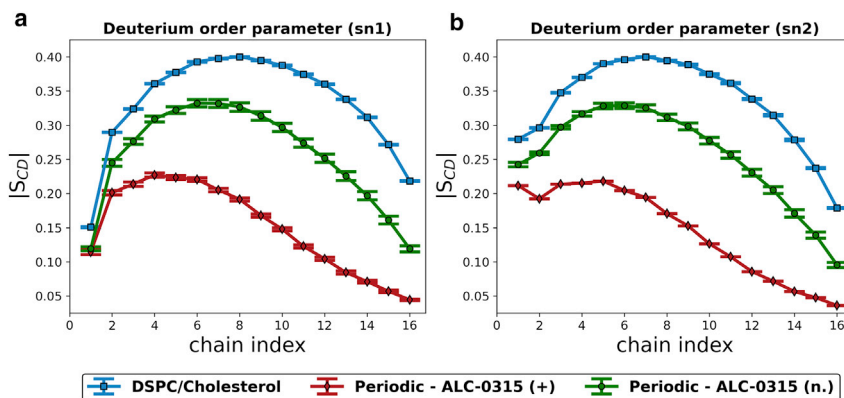


FIGURE 4 The order of three bilayer-like systems was assessed through the deuterium order parameters calculated for the (*a*) *sn1* and the (*b*) *sn2* acyl chains of DSPC. An in-house written script was used to calculate the order parameters according to the local normal of the lipids. The error bars represent the standard error of the mean. To see this figure in color, go online.

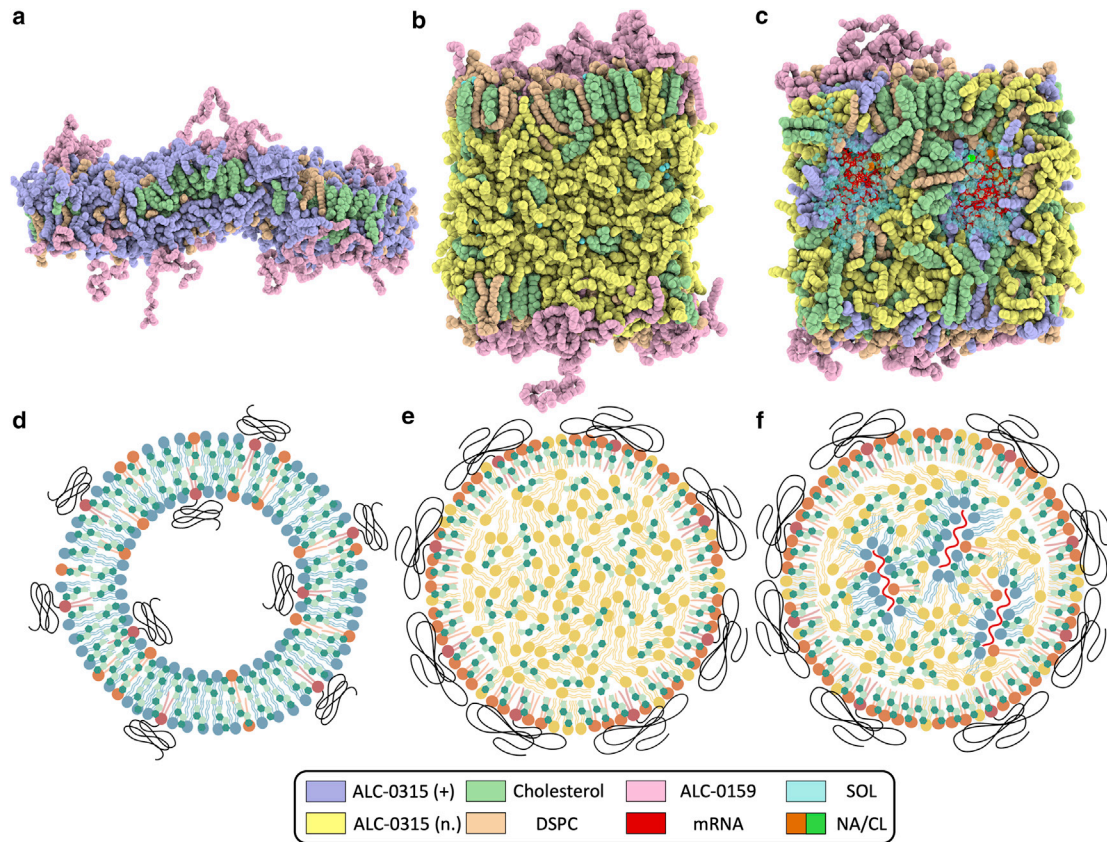


FIGURE 5 Atomistic (*upper panels*) and schematic (*lower panels*) structures of the *Comirnaty* lipid-mRNA mixture derived from self-assembly MD simulations. (a) The protonation of ALC-0315 enables the formation of stable bilayers, implying vesicular structures of unloaded LNPs at a low pH. (b) The deprotonation of ALC-0315 leads to a change of the unilamellar structure toward a LNP membrane with an electron-dense core built by both the deprotonated aminolipid and cholesterol molecules. (c) The addition of mRNA and the partial deprotonation of aminolipids leads to an assimilation of the polynucleotides into the LNP membrane core enveloped mainly by the cationic ALC-0315. Lipids, water, and ions are represented as spheres. mRNA is shown in stick representation. The lower panels show schematic structures for the *Comirnaty* vaccine lipid/mRNA composition. At low pH, these are suggested to form lipid vesicles (d) and LNPs at neutral pH in absence (e) and presence (f) of mRNA. The images were created with PyMol (41) and BioRender.com. To see this figure in color, go online.

PEGs: The deprotonation of the aminolipids results in a bilayer surface area decreased by $\approx 71\%$ (from 734 nm^2 to 210 nm^2), and a thus substantially increased PEG-covered surface of the membrane-like phase ($20.5\% \pm 0.4\%$ of solvent-accessible surface was PEG-covered at low pH, and $58.9\% \pm 0.8\%$ at neutral pH, sketched in Fig. 5, d and e for LNPs). The depletion of aminolipids and cholesterol from the surface additionally induced an increase in the order of DSPC lipids (Fig. 4, a and b, green line).

Self-assembly of *Comirnaty* lipid/mRNA composition

Next the organization of the LNP lipid mixture containing mRNA was studied, based on multiple self-assembly simulations in the presence of short strands of nucleoside-modified mRNA (see materials and methods, similar to the mRNA-free case). The length of the mRNA was chosen to yield an N/P -ratio of around 6 between the positively

charged nitrogen groups (N) of the aminolipids and the negatively charged phosphate groups (P) of the polynucleotide. The same ratio is used in the mixture of the *Comirnaty* vaccine (3).

At low pH, i.e., with protonated aminolipids, we observed a fast adsorption of the aminolipids to the backbone of the mRNA within nanoseconds. Subsequently, a sudden increase in pH to ≈ 7 was modeled by decharging different sets of aminolipids (system E, two replicas each): 1) aminolipids at a distance of $> 1.2 \text{ nm}$ from the mRNA, 2) a similar number of randomly chosen aminolipids, and 3) all aminolipids (see materials and methods). Specifically, for set 1 it is suggested that the pK_a of those aminolipids be close to the negative charge of the mRNA increases based on electrostatic stabilization of the protonated form of the aminolipid. Set 2 investigates for comparison the effect of the specific positioning of protonated aminolipids. Finally, the possibility that all aminolipids are deprotonated also in the presence of mRNA is studied in set 3. For all systems and replicas, the

subsequent equilibration of the systems led to the formation of an oil-like phase sandwiched between two monolayers containing mainly DSPC, the PEGylated lipid, and cholesterol, as described above for the mRNA-free *Comirnaty* lipid composition. The negatively charged mRNA was either completely (three simulations) or partly embedded (one simulation) within the lipid bulk for those systems including protonated aminolipids (Figs. 5 c and S1 a and b). In contrast, the mRNA dissolved into the aqueous phase if all aminolipids were neutralized (Fig. S2, a and b). The latter finding strongly suggests that a partial protonation of the aminolipids is required for mRNA encapsulation in LNPs. Accordingly, for sets 1 and 2, the protonated aminolipids were found to be the main type of lipids around the backbone of the mRNA strands (Fig. 5, c and f; radial distribution function of lipids around mRNA is shown in Fig. S3). Similar to earlier reports (16,19,56), we observed a few DSPC lipids that contributed also to the lipid shell around the nucleotides by interaction of their polar headgroups with the negatively charged backbone of the mRNA. However, most of the phospholipids resided at the interface between the solvent and the apolar bulk phase. In addition to mRNA, the formed caveats were filled by water and ions. During the simulation time, the largely isolated caveats stayed stable and did not coalesce.

Atomistic structure of *Comirnaty* lipid nanoparticles

In the following, the structural characteristics deduced from MD simulations of the *Comirnaty* lipid mixture at neutral pH (Fig. 5 b) was conferred to full, mRNA-free LNPs. The absence of any internal structure within the hydrophobic core of the membrane-like configuration (“LNP membrane,” Fig. 5 b) suggests that the energetically most favorable configuration for *Comirnaty* LNPs is an oil-like phase as a spherical droplet that is surrounded by a lipid monolayer (sketched in Fig. 5 e). Accordingly, the lipid composition of the hydrophobic core of the LNP membrane was used for construction of the LNP core, and the LNP shell was constructed as a monolayer similar to the interfacial layers of the LNP membrane (Fig. 5 b).

Additionally, the LNP membrane was used to estimate the size of mRNA-free LNPs. Assuming a similar surface/vol-

ume ratio for the LNP membrane (Fig. 5 b) and for the full LNPs at neutral pH, the LNP diameter in solution is estimated as 33.7 nm (Fig. 5 e), very close to the diameter of ≈ 40 nm at which LNPs were reported to form bilayer blebs (56).

A similar segregation of a deprotonated aminolipid from phospholipids was also reported previously for other lipid mixtures containing aminolipids using MD simulations (19,53). Cryo-TEM images at pH 7.4 for mixtures containing KC2:DSPC:Chol:PEG-c-DMA (40:11.5:47.5:1 mol %) (16), KC2:DSPC:Chol:PEG-DMG (50:10:38.5:1.5 mol %) (57), and MC3:DSPC:Chol:DMPE-PEG₂₀₀₀ (17) (50:10:38.5:1.5 mol %) further suggested an amorphous core region similar to the one observed here for the aminolipid ALC-0315; at low pH of 4.0, the KC2 aminolipid mixture formed vesicles with a diameter decreasing for increasing KC2 concentrations (57).

Based on the above considerations, a fully atomistic model of a mRNA-free LNP at neutral pH with a diameter of around 35 nm was constructed (systems F and G in Table 1). The iterative setup of the system including in total 7.2 Mio atoms is sketched in Fig. 1 and further detailed in materials and methods.

Upon simulation (simulation length 1.2 μ s), the monolayer surrounding the LNP core equilibrated to a composition for aminolipid:DSPC:cholesterol:ALC-0159 of 8.8:22.3:63.3:5.6 mol % (compare Table 2 and Fig. S4). The very high cholesterol content of 63% remained below the solubility limit of cholesterol in PC bilayers of 66% (58). A high cholesterol content of 51 mol % within the shell was also reported for MC3-LNPs based on modeling of small-angle neutron scattering (SANS) data (18). Differently, however, the model for MC3-LNPs contained a substantially increased amount of aminolipids within the shell (28 mol % vs. 8.8 mol % for the *Comirnaty* LNP).

Almost half of the solvent-accessible surface area of the LNP (system G) ($46.8\% \pm 0.3\%$) is coated with the polymers of the PEGylated lipids (using a probe radius of 0.27 nm). Interestingly, $80.6\% \pm 0.5\%$ of the solvent-accessible surface area of the deprotonated aminolipids within the LNP shell is shielded by the PEG chains. Cholesterol and DSPC at the surface are only covered by $46.8\% \pm 0.6\%$ and $24.4\% \pm 0.4\%$, respectively. The observation that mainly the more hydrophobic aminolipids are coated by

TABLE 2 Distribution of lipids in differently composed LNPs assuming a core-shell structure

	Composition	Molar fractions (mol %)	Core (mol %)	Shell (mol %)
A	ALC-0315:DSPC:Chol:ALC-0159	46.2:9.1:42.4:2.3	71.9:0:28.1:0	8.8:22.3:63.3:5.6
B	DLin-MC3-DMA:DSPC:Chol:DMPE-PEG ₂₀₀₀ :mRNA	50:10:38.5:1.5:0.015	76:0:24:0:0.033	28:18:51:2.7:0
C	DLin-KC2-DMA:DSPC:Chol:PEG-DMG	50:10:38.5:1.5	92:0:8:0	–

Row A shows results derived here from MD simulations of a mRNA-free *Comirnaty* LNP. Data on the composition of LNPs containing DLin-MC3-DMA (abbreviated as MC3-LNPs, B) were reported based on SANS and solubility experiments (18). The scattering length densities and the volume fractions of the components were used to determine their molar fractions under the assumption of a core-shell sphere model (18). The modeled ratio between the aminolipid and cholesterol in the core fits to the solubility limit of cholesterol in DLin-MC3-DMA (17). The core composition of the DLin-KC2-DMA containing LNPs (abbreviated KC2-LNPs, C) was estimated based on the solubility limit of cholesterol within the aminolipid (57).

PEG polymers substantiates the hypothesis that PEGylated lipids might stabilize the structure of LNPs in the absence of a fully enclosing DSPC/cholesterol monolayer as discussed by Kulkarni et al. (57).

The composition of the core domain of the *Comirnaty* LNPs equilibrated within 0.8–1.2 μs to an aminolipid/cholesterol ratio of 1.0:0.39, corresponding to an overall proportion of 28.1 mol % cholesterol (core of LNP membrane at 27.8 mol %, see also Fig. S5), as compared with 24 mol % cholesterol observed for MC3-LNPs (18) and only 8 mol % reported for the solubility of cholesterol in KC2 (57).

Different authors (17,18,57) discussed the possible existence of cholesterol crystals in the core and the shell of LNPs. In our simulations, cholesterol did not show

any indication of crystal formation within the core of the *Comirnaty* LNP as evidenced by the cumulative radial distribution function shown in Fig. 6 b. Similarly, despite the high concentration at the solubility limit, no crystal formation was observed within the LNP shell. However, the high amount of cholesterol within the LNP shell further confines the area occupied by the tails of DSPC and the PEGylated lipids. This results in deuterium order parameters for the DSPC acyl chains within the LNP shell comparable with binary DSPC/cholesterol membrane (Fig. S6, a and b).

Of note, while the suitability of the CHARMM36 force field for the formation of possible cholesterol crystals is not entirely clear, a recent study indicates that the CHARMM36 lipid force field performs well for

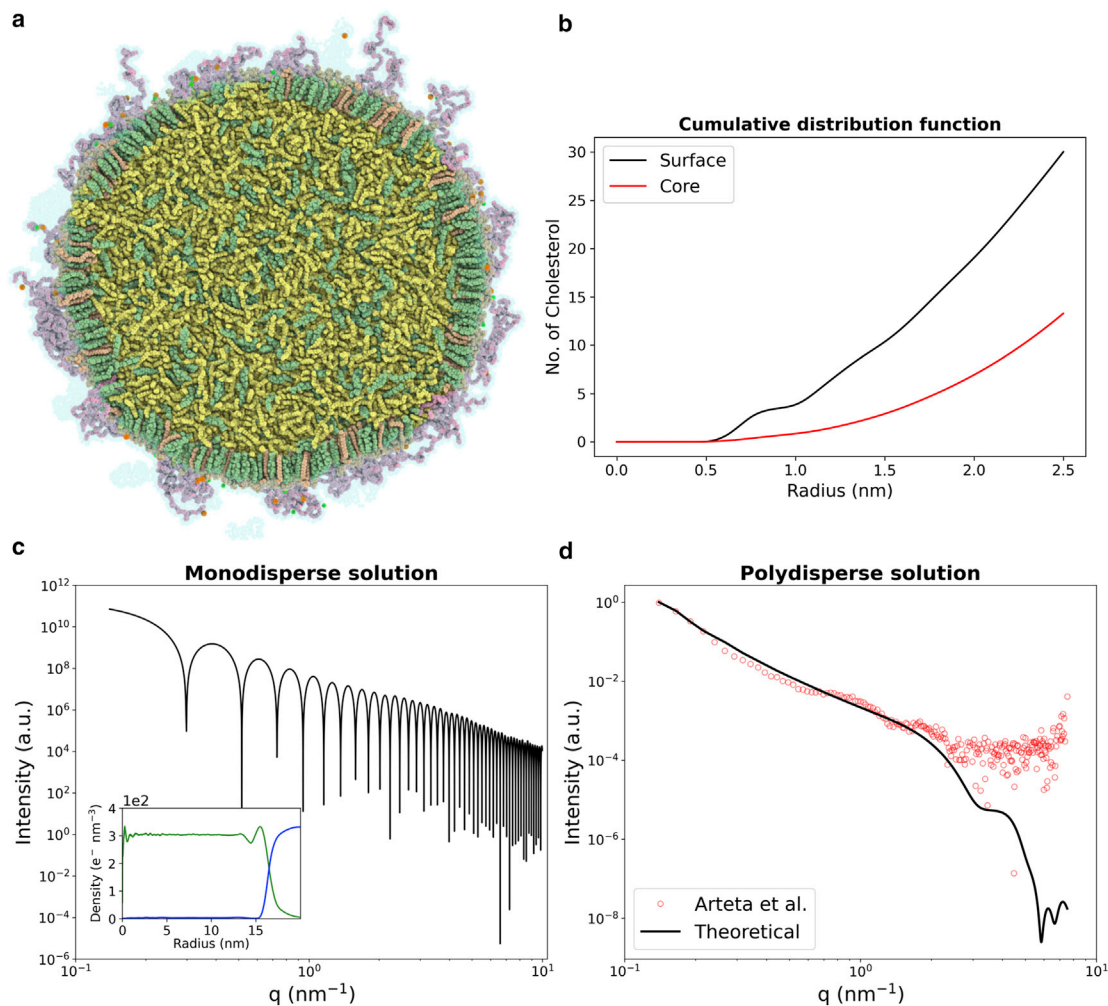


FIGURE 6 (a) Cross section of a lipid nanoparticle with a diameter of ≈ 35 nm. DSPC, cholesterol, and ALC-0159 form a shell around a core composed of the remaining cholesterol and the neutral ALC-0315 (see Fig. 5 for color code). The image was created with PyMol (41). (b) Cumulative distribution function of cholesterol in the core (red line) and the surface (black line) of the lipid nanoparticle. Cholesterol packs more densely on the surface of the lipid nanoparticles, close to the solubility limit. (c) SAXS intensity curve calculated for the LNP model. The inset shows the radial electron densities of the lipids (green line) and of the surrounding solvent (blue line). (d) A comparison between the theoretical prediction of a SAXS curve for a polydisperse LNP solution (black line) and the corresponding experimental SAXS curve (red) for MC3: DSPC: Chol: DMPE-PEG₂₀₀₀ LNPs (17). To see this figure in color, go online.

cholesterol-cholesterol interactions at least up to a concentration of 44 mol % cholesterol in ternary membranes (59).

For comparison with other LNPs, but also for future experimental validation, we analyzed the intensity curve to be expected from SAXS on (mRNA-free) *Comirnaty* LNPs from our simulations. Two approaches were chosen and combined with each other: First, an established protocol for the calculation of SAXS curves from MD simulation trajectories for an LNP of defined size was employed that takes the explicit positions of solute and solvent atoms into account (47). The obtained scattering intensity is the one expected for monodisperse LNPs (Fig. S7). To extend this approach to a polydisperse LNP solution present in experiments, we assumed 1) a continuous electron density and 2) a spherical symmetry of the solvated nanoparticles (see [materials and methods](#)). The continuous electron density yields a decent agreement of the scattering intensity for monodisperse LNPs as compared with the atomistic approach for a q -range below $2 - 3 \text{ nm}^{-1}$ (see Fig. S7). The electron densities for different LNP radii were generated based on the electron density of the simulated LNP (system G) assuming an unaltered density shape for different sizes.

Finally, averaging the scattering intensity for an assumed polydisperse distribution of LNPs employing continuous electron densities allows comparison of theoretical curves obtained for the *Comirnaty* LNPs to experimental SAXS scattering intensities previously reported for MC3:DSPC:Chol:DMPE-PEG₂₀₀₀ nanoparticles (50:10:38.5:1.5 mol %) (17) (Fig. 6 d). Assuming a generalized extreme value distribution for the LNP radii with a most likely radius of $\approx 39.4 \text{ nm}$, the scattering intensities show an excellent agreement for low q -values and diverge for lower correlation lengths (q -values above 2.5 nm^{-1}). This larger radius for MC3-LNPs fits well to LNP size distributions extracted from cryo-TEM (17). The weak additional bump for the experimental scattering intensity at $q \approx 1 \text{ nm}^{-1}$ —i.e., for a correlation length of $\approx 6 \text{ nm}$ —may hint at an internal structure of MC3-LNPs (17) that was absent for the *Comirnaty* LNPs studied here. Likewise, the SAXS pattern of KC2-LNPs did not indicate a structural arrangement of the lipids in the amorphous core region (57).

CONCLUSION

Our investigation outlined some important features of the lipid mixture used in the *Comirnaty* vaccine against the SARS-CoV-2 virus. In its protonated state, i.e., at low pH, the ionizable aminolipid ALC-0315 supports the formation of typical bilayer structures. The composition is characterized by high disorder (19) and substantially enlarged elasticity compared with typical phospholipid bilayers. A phase transition is observed upon deprotonation of the aminolipids at neutral pH, likely resulting in the formation of LNPs. The simulations suggest that these phases separate into a hydrophobic core region formed by the aminolipid and cholesterol

and a surrounding shell formed by a monolayer of DSPC, cholesterol, aminolipids, and surface-covering PEGylated lipids. This outer shell is characterized by a cholesterol concentration close to the solubility limit, a comparably high order of the DSPC acyl chains, a partial coating with PEGylated lipids, and the emergence also of neutral aminolipids. Experimental reports indicated both monolayer-surrounded LNPs (17,57) and multilamellar structures (3,18,45) surrounding the aminolipid-cholesterol phase. Our results obtained on LNP-membrane-like systems and for a full LNP clearly favor an LNP configuration with an oil-like core surrounded by a highly ordered phospholipid monolayer. The PEG chains establish an umbrella-like shield with aminolipids clustering beneath within the outer shell (Fig. 7).

However, we cannot exclude that with growing size (e.g., mRNA loading, different preparation technique, etc.) multilamellar structures appear at the surface of the LNPs due to, for example, an increasing volume-area ratio.

For mRNA-containing LNPs, our results hint mainly at the formation of shielded polar mRNA cavities within the *Comirnaty* LNPs that are stabilized by charged aminolipids. This is in strong contrast to the reported formation of multilamellar lipid structures for KC2 LNPs sandwiching small interfering RNA for a lower N/P ratio (57). Our results are more consistent with a model for mRNA LNPs proposed by Arteta et al. (17), which suggests rigid mRNA-water cylinders within the core of LNPs surrounded by lipids in an inverted hexagonal (H_{II}) phase. Indeed, in one simulation of the LNP membrane starting from a random deprotonation of aminolipids (see Fig. S1 b), the final structure is reminiscent of an inverted hexagonal phase. Our simulations corroborate the necessity of charged aminolipids to stabilize mRNA-lipid complexes within the apolar core of the *Comirnaty* LNPs during the transition from low to neutral pH.

The size of *Comirnaty* vaccine LNPs containing a full-length mRNA strand can be estimated by multiplying the volume of the mRNA-containing LNP-membrane systems (excluding water, Fig. 5 c) with the ratio between the

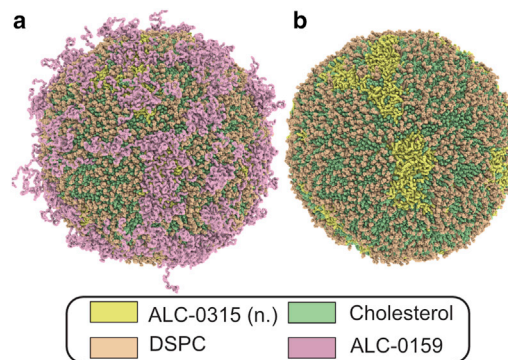


FIGURE 7 Representative snapshot of the LNP displayed (a) with and (b) without the PEGylated lipid (ALC-0159). The images were created with PyMol (41). To see this figure in color, go online.

number of nucleotides in the vaccine (≈ 4000 (38)) and in the simulations (80; the N/P ratio between vaccine and simulation is similar). This rough calculation yields an average diameter of ≈ 50 nm for *Comirnaty* vaccine LNPs with one mRNA strand, compared with ≈ 35 nm for the mRNA-free LNPs (see above). Nanoparticles of this size would harbor a $\approx 47\%$ increase of phospholipids per area. Thus, even for larger *Comirnaty* nanoparticles, the formation of bilayers shielding the core appears unlikely, all the more as the phospholipid content is not even sufficient for establishing a closed phospholipid monolayer for the small LNPs studied here and as phospholipids contribute to mRNA shielding within the LNP core as well.

Methodologically, limited by poor scaling of constant pH simulations with the number of titratable sites, we here employed an instantaneous deprotonation of the aminolipids corresponding to a global switch in pH from low pH to neutral pH (at low pH all titratable sites are exposed to the solvent). In the near future, scalable constant pH simulations (60) will likely enable us to study as well reverse smooth pH transitions for systems as large as LNPs from neutral to low pH corresponding to the situation in endosomes.

Regarding processes following administration of LNPs loaded with mRNA, the surface of the LNP usually becomes coated with a biomolecular corona composed of different proteins influencing the distribution, the circulation time, and the transfection efficiency of the nanoparticle (61–63). Apolipoprotein E (ApoE) plays, for example, a major role in the uptake of LNPs and liposomes into hepatocytes (64–66). Sebastiani et al. (18) measured fast binding kinetics of ApoE to LNPs and proposed that the presence of ApoE induces even an increased cholesterol level within the LNP surface. The observed formation of large solvent-accessible DSPC/cholesterol domains at the surface of the *Comirnaty* LNP could represent a preferential binding site for ApoE. Hence, we think that the headgroup of the titratable aminolipid seems to play a minor role in the initial binding of ApoE at the LNP surface.

mRNA release following cellular internalization of loaded LNPs, trapping in endosomes, and endosomal maturation with a concomitant decrease in pH is probably initiated by protonation of ALC-0315 aminolipids readily accessible within the LNP shell (Fig. S1). Coarse-grained MD simulations by Bruininks et al. (67) focused on the escape of double-stranded DNA from an H_{II} phase formed in combination with a binary mixture of cationic lipids and standard phospholipids (so-called lipoplexes). They showed that the formation of a fusion stalk between the endosomal membrane and a lipoplex followed by an unzipping of the H_{II} phase initiates the release of the polynucleotides. However, their results cannot be fully transferred to the systems in the present work owing to the differences in composition of the delivery systems. Using single-molecule localization microscopy experiments, mRNA release from

recycling tubules of the early endosome was recently shown to depend on accumulation in the tubules (68). Additionally, images of single mRNA escape events indicated a disassembly of the LNPs in the early endosome releasing the mRNA first into the endosomal lumen. ALC-0315 aminolipids, either freely diffusing or bound to the released mRNA, with their pronounced cone-like structure, will accumulate in regions of the tubules with negative curvature. This supports the formation of a membrane-destabilizing H_{II} phase (69,70) inducing membrane leakage to facilitate mRNA escape into the cytoplasm. The recharging of the aminolipids within the LNP shell is therefore likely to destabilize the nanoparticle by reversal of the aforementioned phase transition. The titratable aminolipid ALC-0315 thus acts as a highly cooperative molecular switch to dismantle the integrity of the LNP as well as to reduce the potential barrier for mRNA escape.

SUPPORTING MATERIAL

Supporting material can be found online at <https://doi.org/10.1016/j.bpj.2022.08.037>.

AUTHOR CONTRIBUTIONS

R.A.B. and M.T. designed the research. M.T. carried out all simulations and analyzed the data. R.A.B. and M.T. wrote the article.

ACKNOWLEDGMENTS

The authors thank Marianna Yanez Arteta for providing SAXS data for MC3-LNPs (17) and gratefully acknowledge the computer resources and support provided by the Erlangen Regional Computing Center (RRZE) and the Erlangen National High Performance Computing Center (NHR@FAU).

DECLARATION OF INTERESTS

The authors declare no competing interests.

REFERENCES

1. Malone, R. W., P. L. Felgner, and I. M. Verma. 1989. Cationic liposome-mediated RNA transfection. *Proc. Natl. Acad. Sci. USA.* 86:6077–6081.
2. Kulkarni, J. A., P. R. Cullis, and R. Van Der Meel. 2018. Lipid nanoparticles enabling gene therapies: from concepts to clinical utility. *Nucleic Acid Ther.* 28:146–157.
3. Schoenmaker, L., D. Witzigmann, ..., D. J. A. Crommelin. 2021. mRNA-lipid nanoparticle COVID-19 vaccines: structure and stability. *Int. J. Pharm.* 601:120586.
4. Ansell, S. M., and X. Du. 2015. Novel Lipids and Lipid Nanoparticle Formulations for Delivery of Nucleic Acids. <https://patents.google.com/patent/WO2017075531A1/en>.
5. Sabnis, S., E. S. Kumarasinghe, ..., K. E. Benenato. 2018. A novel amino lipid series for mRNA delivery: improved endosomal escape and sustained pharmacology and safety in non-human primates. *Mol. Ther.* 26:1509–1519.

6. Semple, S. C., S. K. Klimuk, ..., P. Scherrer. 2001. Efficient encapsulation of antisense oligonucleotides in lipid vesicles using ionizable aminolipids: formation of novel small multilamellar vesicle structures. *Biochim. Biophys. Acta.* 1510:152–166.
7. Semple, S. C., A. Akinc, ..., M. J. Hope. 2010. Rational design of cationic lipids for siRNA delivery. *Nat. Biotechnol.* 28:172–176.
8. Guevara, M. L., F. Persano, and S. Persano. 2020. Advances in lipid nanoparticles for mRNA-based cancer immunotherapy. *Front. Chem.* 8:589959.
9. Ge, X., L. Chen, ..., W. Yuan. 2020. Rationale and application of PE-Gylated lipid-based system for advanced target delivery of siRNA. *Front. Pharmacol.* 11:598175.
10. Reichmuth, A. M., M. A. Oberli, ..., D. Blankschtein. 2016. mRNA vaccine delivery using lipid nanoparticles. *Ther. Deliv.* 7:319–334.
11. WHO. 2020. COVID-19 Strategy Update. World Health Organization.
12. Walls, A. C., Y. J. Park, ..., D. Veelsler. 2020. Structure, function, and antigenicity of the SARS-CoV-2 spike glycoprotein. *Cell.* 183:1735–2292.
13. Wrapp, D., N. Wang, ..., J. S. McLellan. 2020. Cryo-EM structure of the 2019-nCoV spike in the prefusion conformation. *Science.* 367:1260–1263.
14. Polack, F. P., S. J. Thomas, ..., C4591001 Clinical Trial Group. 2020. Safety and efficacy of the BNT162b2 mRNA covid-19 vaccine. *N. Engl. J. Med.* 383:2603–2615.
15. Baden, L. R., H. M. El Sahly, ..., T. Zaks. 2021. Efficacy and safety of the mRNA-1273 SARS-CoV-2 vaccine. *N. Engl. J. Med.* 384:403–416.
16. Leung, A. K. K., I. M. Hafez, ..., P. R. Cullis. 2012. Lipid nanoparticles containing siRNA synthesized by microfluidic mixing exhibit an electron-dense nanostructured core. *J. Phys. Chem. C Nanomater. Interfaces.* 116:18440–18450.
17. Yanez Arteta, M., T. Kjellman, ..., L. Lindfors. 2018. Successful reprogramming of cellular protein production through mRNA delivered by functionalized lipid nanoparticles. *Proc. Natl. Acad. Sci. USA.* 115:E3351–E3360.
18. Sebastiani, F., M. Yanez Arteta, ..., M. Cárdenas. 2021. Apolipoprotein E binding drives structural and compositional rearrangement of mRNA-containing lipid nanoparticles. *ACS Nano.* 15:6709–6722.
19. Paloncýová, M., P. Čechová, ..., M. Otyepka. 2021. Role of ionizable lipids in SARS-CoV-2 vaccines as revealed by molecular dynamics simulations: from membrane structure to interaction with mRNA fragments. *J. Phys. Chem. Lett.* 12:11199–11205.
20. Buschmann, M. D., M. J. Carrasco, ..., D. Weissman. 2021. Nanomaterial delivery systems for mRNA vaccines. *Vaccines.* 9:65.
21. Dolgin, E. 2021. The tangled history of mRNA vaccines. *Nature.* 597:318–324.
22. Klauda, J. B., R. M. Venable, ..., R. W. Pastor. 2010. Update of the CHARMM all-atom additive force field for lipids: validation on six lipid types. *J. Phys. Chem. B.* 114:7830–7843.
23. Yu, Y., and J. B. Klauda. 2020. Update of the CHARMM36 united atom chain model for hydrocarbons and phospholipids. *J. Phys. Chem. B.* 124:6797–6812.
24. Vanommeslaeghe, K., and A. D. MacKerell, Jr. 2012. Automation of the CHARMM General Force Field (CGenFF) I: bond perception and atom typing. *J. Chem. Inf. Model.* 52:3144–3154.
25. Vanommeslaeghe, K., E. P. Raman, and A. D. MacKerell, Jr. 2012. Automation of the CHARMM General Force Field (CGenFF) II: assignment of bonded parameters and partial atomic charges. *J. Chem. Inf. Model.* 52:3155–3168.
26. Nosé, S. 1984. A unified formulation of the constant temperature molecular dynamics methods. *J. Chem. Phys.* 81:511–519.
27. Hoover, W. G. 1985. Canonical dynamics: equilibrium phase-space distributions. *Phys. Rev. A Gen. Phys.* 31:1695–1697.
28. Berendsen, H. J. C., J. P. M. Postma, ..., J. R. Haak. 1984. Molecular dynamics with coupling to an external bath. *J. Chem. Phys.* 81:3684–3690.
29. Parrinello, M., and A. Rahman. 1981. Polymorphic transitions in single crystals: a new molecular dynamics method. *J. Appl. Phys.* 52:7182–7190.
30. Darden, T., D. York, and L. Pedersen. 1993. Particle mesh Ewald: an Nlog(N) method for Ewald sums in large systems. *J. Chem. Phys.* 98:10089–10092.
31. Hess, B., H. Bekker, ..., J. G. E. M. Fraaije. 1997. LINCS: a linear constraint solver for molecular simulations. *J. Comput. Chem.* 18:1463–1472.
32. Jorgensen, W. L., J. Chandrasekhar, ..., M. L. Klein. 1983. Comparison of simple potential functions for simulating liquid water. *J. Chem. Phys.* 79:926–935.
33. Lindahl, E., M. Abraham, ..., D. van der Spoel. 2019. GROMACS 2019.3 Source Code. <https://doi.org/10.5281/zenodo.3243833>.
34. Michaud-Agrawal, N., E. J. Denning, ..., O. Beckstein. 2011. MDA-analysis: a toolkit for the analysis of molecular dynamics simulations. *J. Comput. Chem.* 32:2319–2327.
35. Gowers, R. J., M. Linke, ..., I. M. Kenney. 2019. MDAnalysis: A Python Package for the Rapid Analysis of Molecular Dynamics Simulations. Los Alamos National Lab. (LANL), Technical report.
36. Moncelli, M. R., L. Becucci, and R. Guidelli. 1994. The intrinsic pKa values for phosphatidylcholine, phosphatidylethanolamine, and phosphatidylserine in monolayers deposited on mercury electrodes. *Biophys. J.* 66:1969–1980.
37. Case, D. A., D. Cerutti, ..., N. E. A. Homeyer. 2016. AMBER16 Package. University of California.
38. WHO. 2020. INN - 11889. WHO - International Nonproprietary Names Programme. WHO.
39. Denning, E. J., U. D. Priyakumar, ..., A. D. Mackerell, Jr. 2011. Impact of 2'-hydroxyl sampling on the conformational properties of RNA: update of the CHARMM all-atom additive force field for RNA. *J. Comput. Chem.* 32:1929–1943.
40. Xu, Y., K. Vanommeslaeghe, ..., L. Nilsson. 2016. Additive CHARMM force field for naturally occurring modified ribonucleotides. *J. Comput. Chem.* 37:896–912.
41. Schrödinger, L. L. C. 2021. The PyMOL Molecular Graphics System, Version 2.5.0. <https://github.com/schrodinger/pymol-open-source>.
42. Bussi, G., D. Donadio, and M. Parrinello. 2007. Canonical sampling through velocity rescaling. *J. Chem. Phys.* 126:014101.
43. Lindahl, E., M. Abraham, ..., D. van der Spoel. 2021. GROMACS 2021.4 Source Code. <https://doi.org/10.5281/zenodo.5636567>.
44. Ponti, A. 1999. Simulation of magnetic resonance static powder line-shapes: a quantitative assessment of spherical codes. *J. Magn. Reson.* 138:288–297.
45. Patel, S., N. Ashwanikumar, ..., G. Sahay. 2020. Naturally-occurring cholesterol analogues in lipid nanoparticles induce polymorphic shape and enhance intracellular delivery of mRNA. *Nat. Commun.* 11:3435.
46. Park, S., J. P. Bardhan, ..., L. Makowski. 2009. Simulated x-ray scattering of protein solutions using explicit-solvent models. *J. Chem. Phys.* 130:134114-1–134114-8.
47. Chen, P. C., and J. S. Hub. 2014. Validating solution ensembles from molecular dynamics simulation by wide-angle X-ray scattering data. *Biophys. J.* 107:435–447.
48. Guinier, A., G. Fournet, and K. L. Yudowitch. 1955. Small-angle Scattering of X-Rays. Wiley.
49. Virtanen, P., R. Gommers, ..., SciPy 10 Contributors. 2020. SciPy 1.0: fundamental algorithms for scientific computing in Python. *Nat. Methods.* 17:261–272.
50. Canham, P. B. 1970. The minimum energy of bending as a possible explanation of the biconcave shape of the human red blood cell. *J. Theor. Biol.* 26:61–81.
51. Helfrich, W. 1973. Elastic properties of lipid bilayers: theory and possible experiments. *Z. Naturforsch. C Biosci.* 28:693–703.

52. Levine, Z. A., R. M. Venable, ..., F. L. H. Brown. 2014. Determination of biomembrane bending moduli in fully atomistic simulations. *J. Am. Chem. Soc.* 136:13582–13585.
53. Ramezanpour, M., M. L. Schmidt, ..., D. P. Tieleman. 2019. Ionizable amino lipid interactions with POPC: implications for lipid nanoparticle function. *Nanoscale*. 11:14141–14146.
54. Ipsen, J. H., G. Karlström, ..., M. J. Zuckermann. 1987. Phase equilibria in the phosphatidylcholine-cholesterol system. *Biochim. Biophys. Acta*. 905:162–172.
55. Rawicz, W., K. C. Olbrich, ..., E. Evans. 2000. Effect of chain length and unsaturation on elasticity of lipid bilayers. *Biophys. J.* 79:328–339.
56. Kulkarni, J. A., D. Witzigmann, ..., P. R. Cullis. 2019. On the role of helper lipids in lipid nanoparticle formulations of siRNA. *Nanoscale*. 11:21733–21739.
57. Kulkarni, J. A., M. M. Darjuan, ..., P. R. Cullis. 2018. On the formation and morphology of lipid nanoparticles containing ionizable cationic lipids and siRNA. *ACS Nano*. 12:4787–4795.
58. Huang, J., J. T. Buboltz, and G. W. Feigenson. 1999. Maximum solubility of cholesterol in phosphatidylcholine and phosphatidylethanolamine bilayers. *Biochim. Biophys. Acta*. 1417:89–100.
59. Elkins, M. R., A. Bandara, ..., M. Hong. 2021. Direct observation of cholesterol dimers and tetramers in lipid bilayers. *J. Phys. Chem. B*. 125:1825–1837.
60. Aho, N., P. Buslaev, ..., B. Hess. 2022. Scalable Constant pH Molecular Dynamics in GROMACS. ChemRxiv.
61. Francia, V., R. M. Schiffelers, ..., D. Witzigmann. 2020. The biomolecular corona of lipid nanoparticles for gene therapy. *Bioconjugate Chem.* 31:2046–2059.
62. Monopoli, M. P., C. Aberg, ..., K. A. Dawson. 2012. Biomolecular coronas provide the biological identity of nanosized materials. *Nat. Nanotechnol.* 7:779–786.
63. Cullis, P. R., A. Chonn, and S. C. Semple. 1998. Interactions of liposomes and lipid-based carrier systems with blood proteins: relation to clearance behaviour in vivo. *Adv. Drug Deliv. Rev.* 32:3–17.
64. Akinc, A., W. Querbes, ..., M. A. Maier. 2010. Targeted delivery of RNAi therapeutics with endogenous and exogenous ligand-based mechanisms. *Mol. Ther.* 18:1357–1364.
65. Bisgaier, C. L., M. V. Siebenkas, and K. J. Williams. 1989. Effects of apolipoproteins A-IV and A-I on the uptake of phospholipid liposomes by hepatocytes. *J. Biol. Chem.* 264:862–866.
66. Yan, X., F. Kuipers, ..., J. A. A. M. Kamps. 2005. The role of apolipoprotein E in the elimination of liposomes from blood by hepatocytes in the mouse. *Biochem. Biophys. Res. Commun.* 328:57–62.
67. Bruininks, B. M., P. C. Souza, ..., S. J. Marrink. 2020. A molecular view on the escape of lipoplexed DNA from the endosome. *Elife*. 9:e52012.
68. Paramasivam, P., C. Franke, ..., M. Zerial. 2022. Endosomal escape of delivered mRNA from endosomal recycling tubules visualized at the nanoscale. *J. Cell Biol.* 221:e202110137.
69. Cullis, P. R., and B. de Kruijff. 1979. Lipid polymorphism and the functional roles of lipids in biological membranes. *Biochim. Biophys. Acta*. 559:399–420.
70. Hafez, I. M., N. Maurer, and P. R. Cullis. 2001. On the mechanism whereby cationic lipids promote intracellular delivery of polynucleic acids. *Gene Ther.* 8:1188–1196.